nature physics

ARTICLES

https://doi.org/10.1038/s41567-018-0246-1

Topolectrical-circuit realization of topological corner modes

Stefan Imhof[1], Christian Berger[1], Florian Bayer[1], Johannes Brehm[1], Laurens W. Molenkamp[1], Tobias Kiessling[1], Frank Schindler[2], Ching Hua Lee[3,4], Martin Greiter[5], Titus Neupert[2] and Ronny Thomale[5*]

Quantized electric quadrupole insulators have recently been proposed as novel quantum states of matter in two spatial dimensions. Gapped otherwise, they can feature zero-dimensional topological corner mid-gap states protected by the bulk spectral gap, reflection symmetries and a spectral symmetry. Here we introduce a topolectrical circuit design for realizing such corner modes experimentally and report measurements in which the modes appear as topological boundary resonances in the corner impedance profile of the circuit. Whereas the quantized bulk quadrupole moment of an electronic crystal does not have a direct analogue in the classical topolectrical-circuit framework, the corner modes inherit the identical form from the quantum case. Due to the flexibility and tunability of electrical circuits, they are an ideal platform for studying the reflection symmetry-protected character of corner modes in detail. Our work therefore establishes an instance where topolectrical circuitry is employed to bridge the gap between quantum theoretical modelling and the experimental realization of topological band structures.

The Berry phase provides a powerful means to describe the topological character of band structures and single-particle systems[1,2]. It allows one to treat fermionic and bosonic quantum systems on the same footing. Furthermore, the Berry phase concept is not restricted to Hilbert space, but applies to the connectivity of any given coordinate space, and as such accounts for classical degrees of freedom as well[3]. It is thus intuitive that, with the discovery of various topological quantum states of matter such as the quantum Hall[4] and quantum spin Hall effects[5], classical systems with similar phenomenology could also be identified. This was first explored in the context of photonics[6,7], and subsequently transferred to other fields such as mechanics[8,9], acoustics[10] and electronics[11,12], among others. Even though the spectra and eigenstates of the single-particle problem, including edge modes, might look similar or even identical, it is the fundamental degrees of freedom that pose the central distinction between quantum systems and their designed classical analogues. First, quantization phenomena deriving from topological invariants usually necessitate non-commutativity of phase space, and as such are often restricted to quantum systems. Second, internal symmetries pivotal to the protection of a topological phase might not carry over to classical systems as the degrees of freedom are changed from fermionic to effectively bosonic at the single-particle level. For instance, this applies to time-reversal symmetry T, as the protecting symmetry of the quantum spin Hall effect, where the half-integer spin of electrons implies Kramer's degeneracy due to $T^2=-1$ in the quantum case, whereas it does not in the classical case ($T^2=1$). Although the classical counterpropagating edge modes might still be detectable, there is no special topological protection left, rendering the classical system much more vulnerable to perturbations[13].

From this perspective, at least two directions appear the most promising to develop classical topological band structure models that are universally stable beyond fine-tuning. The first is the realization of classical analogues to topological semimetals[14–19], where the extensive edge mode degeneracy suggests clear, persistent spectral edge features also in the presence of small perturbations. The second is to focus on topologically insulating quantum electronic states where either no protecting symmetries are needed, such as the quantum Hall effect[6], or where the protecting symmetries obey the same algebraic relations in both the classical and quantum mechanical cases.

Electric quadrupole insulators[20] fall into the latter category. Whereas the quantum case is most suitably constructed from the viewpoint of quantized multipole moments of an electronic crystal, the complementary protecting-symmetry perspective is the most intuitive for classical system design. The symmetry group that protects quantization of the quadrupole moment includes two non-commuting reflection symmetries M_x and M_y as well as a C_4 rotation symmetry. In particular, they obey $M_{x,y}^2=1$, and as such carry over directly to the classical degrees of freedom. In analogy to the relation between the quantization of the bulk dipole moment (which is quantized to half-integer values by inversion symmetry) and the appearance of protected end states in the topological Su–Schrieffer–Heeger (SSH) model, an additional spectral symmetry, the chiral symmetry, is needed to pin the topological boundary modes in the middle of the bulk energy gap. All these symmetries are realized in the microscopic model given in ref. [20]. Hence, the only task is to implement the hopping model given by a four-site unit cell and real, but sign-changing, hybridization elements. Due to recent progress in implementing waveguide elements that invert the sign of hybridization[21], the complexity of this model has been captured by a photonic cavity lattice structure[22]. Here we will use topolectrical circuits to realize the quadrupole insulators in a classical environment.

Linear circuit theory and topology

We consider non-dissipative linear electric circuits—that is, circuits made of capacitors and inductors. Labelling the nodes of a circuit

[1]Experimentelle Physik 3, Physikalisches Institut, University of Würzburg, Würzburg, Germany. [2]Department of Physics, University of Zurich, Zurich, Switzerland. [3]Institute of High Performance Computing, Singapore, Singapore. [4]Department of Physics, National University of Singapore, Singapore, Singapore. [5]Institute for Theoretical Physics and Astrophysics, University of Würzburg, Würzburg, Germany. *e-mail: rthomale@physik.uni-wuerzburg.de

by $a=1, 2, \ldots$, the response of the circuit at frequency ω is given by Kirchhoff's law

$$I_a(\omega)=\sum_{b=1,2,\cdots} J_{ab}(\omega)V_b(\omega) \tag{1}$$

which relates the voltages V_a to the currents I_a via the grounded circuit Laplacian

$$J_{ab}(\omega)=i\omega C_{ab}-\frac{i}{\omega}W_{ab} \tag{2}$$

Here, the off-diagonal components of the matrix C contain the capacitances C_{ab} between nodes $a\neq b$, whereas the diagonal components are given by the total node capacitance

$$C_{aa}=-C_{a0}-\sum_{b=1,2,\cdots} C_{ab} \tag{3}$$

including the capacitance C_{a0} between node a and the ground. Similarly, the off-diagonal components of the matrix W contain the inverse inductivity $W_{ab}=L_{ab}^{-1}$ between nodes $a\neq b$, whereas the diagonal components are given by the total node inductivity

$$W_{aa}=-L_{a0}^{-1}-\sum_{b=1,2,\cdots} L_{ab}^{-1} \tag{4}$$

including the inductivity L_{a0} between node a and the ground.

At fixed frequency ω, $J_{ab}(\omega)$ determines the linear response of the circuit, in that the impedance Z_{ab} between two nodes a and b is given by

$$Z_{ab}(\omega)=G_{aa}(\omega)+G_{bb}(\omega)-G_{ab}(\omega)-G_{ba}(\omega) \tag{5}$$

where $G(\omega)=J^{-1}(\omega)$ is the circuit Green's function. The impedance is thus dominated by the smallest eigenvalues $j_n(\omega)$ of $J(\omega)$ at this given frequency, provided that the sites a and b are in the support of the corresponding eigenfunctions.

In turn, the frequencies ω for which an exact zero eigenvalue $j_n(\omega)=0$ exists correspond to eigenmodes of the circuit. They are determined by the equations of motion satisfied by the electric potential $\phi_a(t)$ at node a

$$\sum_{b=1,2,\cdots} C_{ab}\frac{\mathrm{d}^2}{\mathrm{d}t^2}\phi_b(t)+\sum_{b=1,2,\cdots} W_{ab}\phi_b(t)=0 \tag{6}$$

The spectrum ω^2 of eigenmodes of the circuit is thus given by the spectrum of the dynamical matrix

$$D=C^{-1/2}WC^{-1/2} \tag{7}$$

where matrix multiplication is implied.

We now explain why topological properties can be defined for the matrices $J(\omega)$ and D that describe the physics of the circuit. To define the topological properties of a physical system, the notions of locality and adiabaticity (enabled by spectral gaps) are of central importance. Locality naturally arises when we consider circuits in which the nodes a are arranged in a (in the case at hand, two-dimensional) lattice. This also allows one to define spatial symmetry transformations. Adiabaticity in turn follows from the spectral continuity of $J(\omega)$ as a function of ω—that is, if a specific frequency ω_0 lies in a gap in the spectrum of D then the spectrum of $J(\omega_0)$ also has a gap around zero eigenvalues. Furthermore, a spectrally isolated eigenvalue (which may be a topological bound state) of D at frequency ω_0 corresponds to a spectrally isolated zero mode of $J(\omega_0)$.

Due to these relations between $J(\omega)$ and D, protected boundary modes of a circuit can arise from the topological properties of either matrix. In this work, we choose to build a two-dimensional circuit for which the topology of $J(\omega_0)$ at a specific frequency ω_0 protects corner modes. The topological protection of spectrally isolated zero modes always requires a spectral (chiral or particle–hole) symmetry that relates eigenvalues of equal magnitude and opposite sign. Spectrally and locally isolated eigenstates of this symmetry, if present, are protected in that they are pinned to an eigenvalue of zero. As an eigenstate of $J(\omega)$, such a state naturally dominates the linear response of the circuit.

Circuit with corner states

To realize a quadrupole insulator with topologically protected corner states, the system should have two anticommuting mirror symmetries, as well as a C_4 rotation symmetry in the bulk. The fundamental mirror symmetries in classical systems commute. To build a classical analogue of a electric quadrupole insulator, we thus devise a circuit that has an emergent pair of anticommuting mirror symmetries M_x and M_y for modes near a specific frequency ω_0. This means that $J(\omega_0)$ commutes exactly with M_x and M_y and the eigenspaces of D are approximately invariant under M_x and M_y for frequencies near ω_0.

We first discuss the bulk properties of a periodically repeating circuit unit cell, depicted in Fig. 1, before considering boundary modes. The circuit unit cell contains four sites denoted by labels $a=1$ ... 4. We use two pairs of capacitors and inductors (C_1, L_1) and (C_2, L_2), which have the same resonance frequency $\omega_0=1/\sqrt{L_1C_1}=1/\sqrt{L_2C_2}$, to couple these sites. The latter equality is automatically satisfied if we set $C_2=\lambda C_1$, $L_2=L_1/\lambda$ for some real positive parameter λ. Sites 1 and 4 are connected to the ground via an LC circuit with $C_1^{\mathrm{g}}=C_1$ and $L_1^{\mathrm{g}}=L_1$ such that it has the same resonance frequency ω_0. Sites 2 and 3 are connected to the ground via an inductivity $L_2^{\mathrm{g}}=L_1/[2(1+\lambda)]$. In this set-up, the circuit is parametrized by the parameters ω_0 and λ.

We now describe the circuit with periodic boundary conditions in momentum space. The Fourier components of the matrix $J_\lambda(\omega)$, denoted by $\tilde{J}_\lambda(\omega,\mathbf{k})$, are 4×4 matrices that satisfy

$$\begin{aligned} M_x\tilde{J}_\lambda(\omega_0,k_x,k_y)M_x^{-1}&=\tilde{J}_\lambda(\omega_0,-k_x,k_y)\\ M_y\tilde{J}_\lambda(\omega_0,k_x,k_y)M_y^{-1}&=\tilde{J}_\lambda(\omega_0,k_x,-k_y)\\ C_4\tilde{J}_\lambda(\omega_0,k_x,k_y)C_4^{-1}&=\tilde{J}_\lambda(\omega_0,k_y,-k_x) \end{aligned} \tag{8}$$

where $M_x=\sigma_1\tau_3$, $M_y=\sigma_1\tau_1$ and $2C_4=(\sigma_1+i\sigma_2)\tau_0+(\sigma_1-i\sigma_2)(i\tau_2)$ are the representations of the symmetries satisfying $M_xM_y=-M_yM_x$ and $C_4M_xC_4^{-1}=M_y$. Here, σ_μ and τ_μ, with $\mu=0, 1, 2, 3$, are the 2×2 identity matrix and the three Pauli matrices. Note that the circuit is then also invariant under the combined symmetries $M_{x\bar{y}}=C_4M_x$ and $M_{xy}=C_4M_y$ that map $(x, y)\to(-y, -x)$ and $(x, y)\to(y, x)$, respectively. In addition, $\tilde{J}_\lambda(\omega_0,\mathbf{k})$ has a chiral symmetry $\mathcal{C}=\sigma_3\tau_0$, which by $\mathcal{C}\tilde{J}_\lambda(\omega_0,\mathbf{k})\mathcal{C}^{-1}=-\tilde{J}_\lambda(\omega_0,\mathbf{k})$ implies a spectral symmetry. Up to an overall factor of i, the circuit Laplacian $\tilde{J}_\lambda(\omega_0,\mathbf{k})$ takes exactly the same form as the Bloch Hamiltonian matrix of the quadrupole insulator introduced in ref. [20] (see the section 'Impedance response and circuit Green's function' in the Methods). For $\lambda\neq1$ the spectrum of $\tilde{J}(\omega_0,\mathbf{k})$ is gapped, and the gapless point $\lambda=1$ corresponds to a topological phase transition between a quadrupole circuit for $\lambda>1$ and a trivial circuit for $\lambda<1$.

We now turn to a circuit with open boundary conditions to realize topologically protected corner modes. In general, two criteria must be met to realize a topological bulk–boundary correspondence. First, the symmetries that protect the topological character must not be broken by the boundary. Second, the system termination

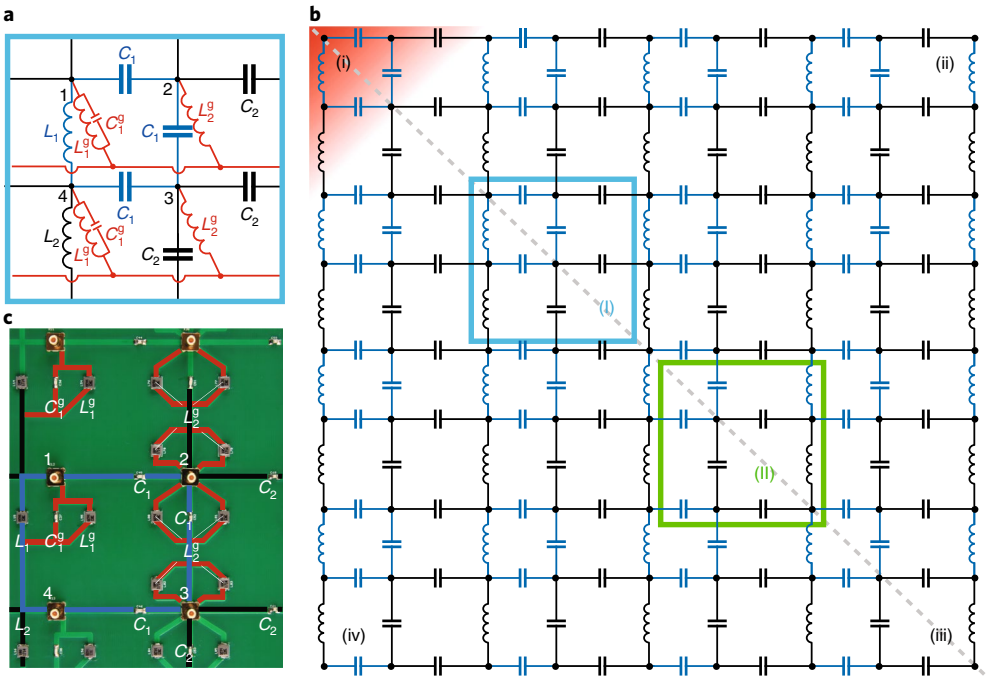

Fig. 1 | Electrical circuit exhibiting a topological corner state with nodes of the circuit indicated by black dots. a, Unit cell of the circuit. Blue and black circuit elements correspond to weak and strong bonds in a tight-binding or mechanical analogue of the circuit. Red circuit elements connect to the ground. All capacitor–inductor pairs have the same resonance frequency $\omega_0 = 1/\sqrt{L_1 C_1} = 1/\sqrt{L_2 C_2} = 1/\sqrt{L_1^g C_1^g}$. **b**, Layout of the full circuit that has been realized experimentally. Double bars denote capacitors and screws denote inductors. The corners (i) and (iii) are invariant under the mirror symmetry that leaves the dashed grey line invariant. They are compatible with the bulk unit cell choices (I) and (II), respectively, indicated by the coloured squares, which correspond to an interchange of strong and weak bonds. As a consequence we expect a topological bound state at corner (i), but not at corner (iii). **c**, Unit cell of the experimentally realized circuit. The unit cell boundary is marked in blue.

must be compatible with the choice of bulk unit cell for which a topological invariant has been defined—that is, the boundary should not cut through unit cells. We demonstrate all of these properties on a single circuit by choosing different boundary terminations as follows. For the open system to obey the chiral symmetry $\mathcal{C}$, the diagonal elements of $J(\omega)$ need to vanish at ω_0. This holds for all bulk sites by the construction of the model. Imposing this symmetry also for edge and corner sites in an open geometry fixes the circuit elements (capacitor and/or inductor) that connect each site to the ground. (See Supplementary Information section D for the specific grounding at the edge termination that was used for the open circuit.)

With this condition imposed on the boundary sites, we terminate the upper left edge of the circuit in a way compatible with the choice of bulk unit cell denoted as (I) in Fig. 1b. The lower right circuit termination is chosen to be compatible with the unit cell denoted as (II) in Fig. 1b. This edge termination preserves the mirror symmetry $M_{x\bar{y}} = C_4 M_x$ and breaks all other spatial symmetries mentioned above. Topological corner modes could thus potentially be protected at the upper left and the lower right corners, which are invariant under $M_{x\bar{y}}$, but not at the other two corners. However, the bulk circuit Laplacians that correspond to the two choices of unit cell (I) and (II) satisfy $\tilde{J}_{\lambda}^{(\mathrm{II})}(\omega_0, \mathbf{k}) = \lambda \tilde{J}_{1/\lambda}^{(\mathrm{I})}(\omega_0, \mathbf{k})$ for an appropriate labelling of unit cell sites. Recalling that the topological phase transition occurs at $\lambda = 1$, this implies that when $\tilde{J}^{(\mathrm{I})}(\omega_0, \mathbf{k})$ is in a topological phase, $\tilde{J}^{(\mathrm{II})}(\omega_0, \mathbf{k})$ is trivial and vice versa. As a result, our choice of boundary termination renders one corner topologically non-trivial (the upper left one for $\lambda > 1$) and the opposite corner trivial.

We thus expect that for $\lambda > 1$ at eigenfrequency ω_0, the circuit depicted in Fig. 1b supports a localized topological corner state at the upper left corner, and none at the lower right or any other corner. We further note that the corner mode should be an exact eigenstate of the $M_{x\bar{y}}$ symmetry. We will now present impedance measurements that support this expectation.

Experimental results

For the experimental realization of topological corner modes a circuit board with 4.5×4.5 unit cells was designed. The line spacing on the board was chosen such that spurious inductive coupling between the circuit elements was below the resolution of our measurements. All impedance measurements were performed with a HP 4194A Impedance/Gain-Phase Analyzer in a full differential configuration. To achieve a clearly resolvable corner state resonance on the superimposed resistive background of the bulk states—that is, the combined impedance contribution of our RLC circuit, which is of the order of a few hundreds of milliohms at the resonance—the values of the circuit elements were chosen to give a resonance frequency of 2.8 MHz. The ratio λ between the capacitors/inductors was set to 3.3, so that the spatially decaying corner state resonance could be observed over three unit cells in each spatial direction (see also Supplementary Information Section B).

Figure 2 compares the experimental data with the theoretical predictions, showing excellent agreement between the two. It demonstrates the existence of a spectrally and spatially localized topological corner state. In Fig. 2a the frequency-dependent spectrum of the circuit Laplacian shows the isolated corner mode and illustrates the connection between a (bulk and edge) spectral gap of $J(\omega)$ at fixed frequency ω and a gap in the spectrum of the dynamical matrix D, which corresponds to a range of frequencies without zero modes of $J(\omega)$. In Fig. 2b, c the corner mode at $\omega = \omega_0$ is mapped out with single-site resolution. The exponential decay of the measured impedance is in excellent agreement with the theoretical expectation

$$\phi_c(x, y) = (-\lambda)^{-(x+y)} \phi_c(0, 0) \tag{9}$$

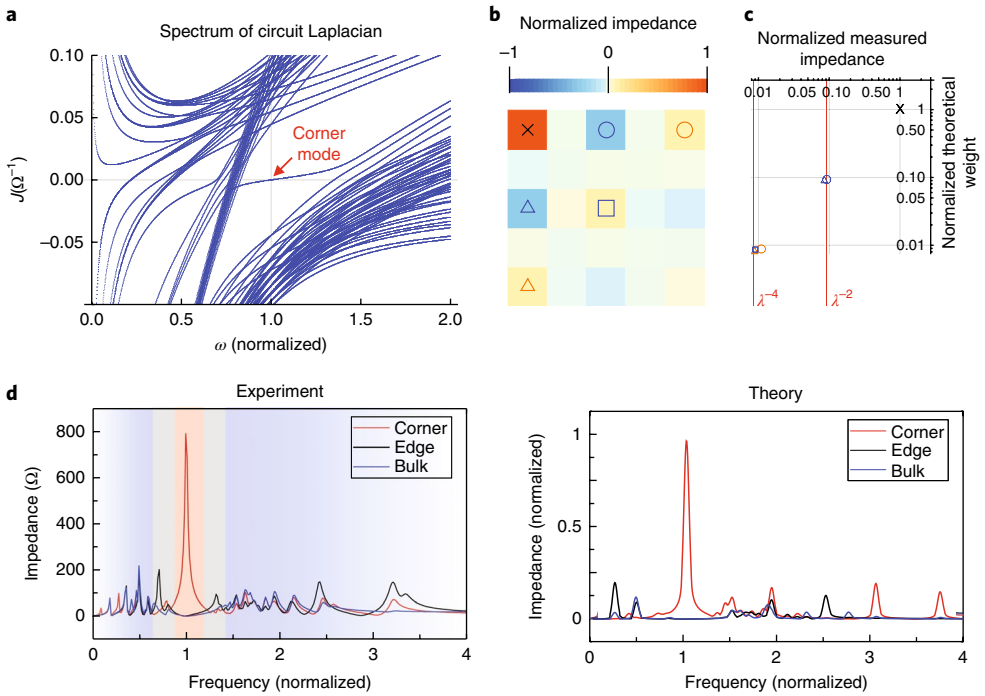

Fig. 2 | Comparison of experimental and theoretical results for the circuit spectrum and corner mode. a, Theoretical spectrum of the circuit Laplacian $J(\omega)$ as a function of the driving frequency. All frequency scales are normalized to the resonance frequency ω_0. An isolated mode crossing the gap, which corresponds to a zero-energy eigenvalue of $J(\omega)$ at $\omega=\omega_0$, is clearly visible. It corresponds to the topological corner mode. The calculation includes a random disorder of 1% for all capacitors and 2% for all inductors. **b**, Theoretical weight distribution of the eigenstate of $J(\omega_0)$ that corresponds to the corner mode (equation (9)), where only the circuit nodes near the corner are shown. **c**, Comparison between the experimental corner mode impedance at $\omega=\omega_0$, measured between nearest-neighbour nodes along the horizontal and vertical edges and along the diagonal, and the theoretically computed weight of the corner mode eigenstate. Both decay with the decay constant $\lambda=3.3$ set by the ratio of alternating capacitors/inductors. **d**, Frequency scan (normalized with respect to ω_0) of the impedance between two nearest-neighbour sites at the corner, at the edge and in the bulk. Both the experimental and theoretical curves show the corner state resonance isolated in the gap of bulk and edge states.

where ϕ_c is the zero-eigenvalue eigenstate of the circuit Laplacian, and $\lambda=C_2/C_1$ according to Fig. 1 and $x,y\in\mathbb{N}$ label the absolute distance from the upper left edge in both spatial directions in units of the circuit lattice constant. The experimental demonstration that the corner mode is indeed spectrally isolated, and as such not due to a bulk or edge effect, is shown in Fig. 2d via a comparison between measurement and simulation. The theoretical impedance corner peak is normalized to unity, with the corresponding impedance corner peak in the actual measurement reaching 800 Ω.

Physical interpretation of corner modes

Along the x and y directions, the circuit corresponds to a collection of connected pairs of linear circuits with alternating capacitors and inductors, respectively. With the appropriate boundary conditions discussed previously, the electric charge on the capacitors forms 'dimerized', isolated oscillators, as described in refs. [19,23]. Note that the capacitances alternate between C_1 and C_2, with $C_1<C_2$, constituting in each direction a one-dimensional SSH model. Such models possess well-known eigenmodes—that is, potential and current profiles where every second node exhibits no current, and accordingly no potential difference[19], which occurs here since a fixed amount of charge Q between each pair of capacitors gives rise to a potential difference $V_1>V_2$, since $Q=V_1C_1=V_2C_2$. With appropriate boundary conditions, we can thus infer the existence of a boundary mode of anti-phase currents that is decaying exponentially by a factor of $1/\lambda=C_1/C_2$ per unit cell.

A novel feature of our measured corner mode is that this mode is not the result of edge polarization—that is, even though the Laplacian eigenstate of the corner mode (equation (9)) suggests a similar form in the x and y directions, it cannot be arrived at by combining SSH models along the different edges. This implies the presence of topological quadrupole polarization in the given circuit, as opposed to dipole polarization in the SSH case. It is instructive to decompose the given circuit in terms of pairs of vertical and horizontal SSH-type circuit chains, where we see both SSH chains built by capacitors as well as their dual form built by inductors in each unit cell chain along the x or y axis. The alternating L-type and C-type SSH chains within the unit cell are then arranged such that their edge charge polarizations cancel. To see this more clearly, we turn to frequency space, where the voltage difference equals Q/C across a capacitor C, but takes the form $L\ddot{Q}\rightarrow-\omega^2LQ$ across an inductor L. By identifying $1/C\equiv-\omega^2L$, we notice that the L-type dual chain possesses effective 'negative couplings' in the Laplacian compared to the C-type chain. For $\omega\rightarrow\omega_0$ this then gives the same absolute but sign-reversed effective coupling, and the dipolar SSH-type polarization cancels out in each unit cell. Physically, the sign difference between the effective couplings of capacitors and inductors results from their opposite quarter-period phase shifts, which add up to a sign reversal.

Discussion

A fundamental difference between classical topological systems (for example, of mechanical degrees of freedom, electrical circuits and photonic metamaterials) and topological insulators made of fermions is that the topology is exhibited in the excitations of classical systems, but not as directly in their bulk response functions as in fermionic systems (see the section 'Dipole and quadrupole polarization' in the Methods for a more detailed discussion.) Consequences of topology in the former case are found in the excitations, whereas

in the latter case, thanks to the Fermi sea that results from the Pauli principle, it is the ground state which is non-trivial. For example, a fermionic electric quantum quadrupole insulator has a quantized bulk quadrupole moment that is an—in principle measurable—characteristic of its (zero-temperature) ground state. (A more canonical example is the bulk Hall conductivity of the integer quantum Hall effect.) In contrast, topological boundary modes are in principle as accessible for measurements in classical as in fermionic quantum systems, since they correspond to spectrally isolated excitations. For this reason, we have focused on the boundary characteristics of the topological circuit in this work.

Note added in proof. During the resubmission process for this work, after our posting on arXiv, two works that report observations of topological corner modes in a mechanical[24] and a microwave photonic[25] system have been published. Furthermore, platforms for bulk measurements of the topological characteristics of classical systems have been suggested in photonic systems[26].

Methods

Methods, including statements of data availability and any associated accession codes and references, are available at https://doi.org/10.1038/s41567-018-0246-1.

Received: 7 September 2017; Accepted: 6 July 2018;
Published online: 4 September 2018

References

1. Berry, M. V. Quantal phase factors accompanying adiabatic changes. *Proc. R. Soc. A* **392**, 45–57 (1984).
2. Zak, J. Berry's phase for energy bands in solids. *Phys. Rev. Lett.* **62**, 2747–2750 (1989).
3. Haldane, F. D. M. Path dependence of the geometric rotation of polarization in optical fibers. *Opt. Lett.* **11**, 730–732 (1986).
4. von Klitzing, K., Dorda, G. & Pepper, M. New method for high-accuracy determination of the fine-structure constant based on quantized Hall resistance. *Phys. Rev. Lett.* **45**, 494–497 (1980).
5. König, M. et al. Quantum spin Hall insulator state in HgTe quantum wells. *Science* **318**, 766–770 (2007).
6. Haldane, F. D. M. & Raghu, S. Possible realization of directional optical waveguides in photonic crystals with broken time-reversal symmetry. *Phys. Rev. Lett.* **100**, 013904 (2008).
7. Wang, Z., Chong, Y., Joannopoulos, J. D. & Soljačić, M. Observation of unidirectional backscattering-immune topological electromagnetic states. *Nature* **461**, 772–775 (2009).
8. Kane, C. L. & Lubensky, T. C. Topological boundary modes in isostatic lattices. *Nat. Phys.* **10**, 39–45 (2014).
9. Süsstrunk, R. & Huber, S. D. Observation of phononic helical edge states in a mechanical topological insulator. *Science* **349**, 47–50 (2015).
10. Yang, Z. et al. Topological acoustics. *Phys. Rev. Lett.* **114**, 114301 (2015).
11. Ningyuan, J., Owens, C., Sommer, A., Schuster, D. & Simon, J. Time-and site-resolved dynamics in a topological circuit. *Phys. Rev. X* **5**, 021031 (2015).
12. Albert, V. V., Glazman, L. I. & Jiang, L. Topological properties of linear circuit lattices. *Phys. Rev. Lett.* **114**, 173902 (2015).
13. Hafezi, M., Demler, E. A., Lukin, M. D. & Taylor, J. M. Robust optical delay lines with topological protection. *Nat. Phys.* **7**, 907–912 (2011).
14. Lu, L., Fu, L., Joannopoulos, J. D. & Soljačić, M. Weyl points and line nodes in gyroid photonic crystals. *Nat. Photon.* **7**, 294–299 (2013).
15. Dubček, T. et al. Weyl points in three-dimensional optical lattices: Synthetic magnetic monopoles in momentum space. *Phys. Rev. Lett.* **114**, 225301 (2015).
16. Lu, L. et al. Experimental observation of Weyl points. *Science* **349**, 622–624 (2015).
17. Rocklin, D. Z., Chen, B. G., Falk, M., Vitelli, V. & Lubensky, T. C. Mechanical Weyl modes in topological Maxwell lattices. *Phys. Rev. Lett.* **116**, 135503 (2016).
18. Noh, J. et al. Experimental observation of optical Weyl points and Fermi arc-like surface states. *Nat. Phys.* **13**, 611–617 (2017).
19. Lee, C. H. et al. Topoelectric circuits. Preprint at https://arXiv.org/abs/1705.01077 (2017).
20. Benalcazar, W. A., Bernevig, B. A. & Hughes, T. L. Quantized electric multipole insulators. *Science* **357**, 61–66 (2017).
21. Keil, R. et al. Universal sign control of coupling in tight-binding lattices. *Phys. Rev. Lett.* **116**, 213901 (2016).
22. Noh, J. et al. Topological protection of photonic mid-gap defect modes. *Nat. Photon.* **12**, 408–415 (2018).
23. Lee, C. H., Li, G., Jin, G., Liu, Y. & Zhang, X. Topological dynamics of gyroscopic and Floquet lattices from Newton's laws. *Phys. Rev. B* **97**, 085110 (2018).
24. Serra-Garcia, M. et al. Observation of a phononic quadrupole topological insulator. *Nature* **555**, 342–345 (2018).
25. Peterson, C. W., Benalcazar, W. A., Hughes, T. L. & Bahl, G. A quantized microwave quadrupole insulator with topologically protected corner states. *Nature* **555**, 346–350 (2018).
26. Ozawa, T. et al. Topological photonics. Preprint at https://arXiv.org/abs/1802.04173 (2018).

Acknowledgements

We thank S. Huber and B. A. Bernevig for discussions. F.S. was supported by the Swiss National Science Foundation. We further acknowledge support by DFG-SFB 1170 TOCOTRONICS (project A07 and B04), by ERC-StG-Thomale- 336012-TOPOLECTRICS, by ERC-AG-3-TOP and by ERC-StG-Neupert-757867-PARATOP.

Author contributions

L.M., S.I., T.K., J.B., C.B. and F.B. were responsible for the circuit implementation and all measurements. F.S., S.I. and T.K. performed numerical simulations of the circuit. R.T., M.G., C.H.L., T.N. and F.S. conceived the project and developed the mapping from a Bloch Hamiltonian to topological circuitry.

Competing interests

The authors declare no competing interests.

Additional information

Supplementary information is available for this paper at https://doi.org/10.1038/s41567-018-0246-1.

Reprints and permissions information is available at www.nature.com/reprints.

Correspondence and requests for materials should be addressed to R.T.

Publisher's note: Springer Nature remains neutral with regard to jurisdictional claims in published maps and institutional affiliations.

Methods

Impedance response and circuit Green's function. The signature of a non-trivial topological phase often lies in its response to an external perturbation. In electronic topological systems, for instance, a non-trivial Chern number corresponds to a non-vanishing quantized Hall response, as epitomized by the Kubo formula. In circuits, however, the Kubo formula does not apply, as there is no quantum excitation from a Fermi sea. Below, we shall derive the appropriate analogue of the Kubo formula for circuits, which is used to characterize the so-called topolectrical response.

Define V_a and I_a to be the voltage and external input current on node a of a circuit. By Kirchhoff's law,

$$\dot{I}_a = C_{ab}\dot{V}_b + W_{ab}V_b \tag{10}$$

where C_{ab} and W_{ab} are the Laplacian matrices of capacitances and inverse inductances, and the summation over repeated indices is implied. For a mode $V(t) \sim V(0)e^{i\omega t}$ at frequency ω, equation (10) takes the form

$$I_a = \left(i\omega C_{ab} - \frac{i}{\omega}W_{ab}\right)V_b = J_{ab}(\omega)V_b \tag{11}$$

where $J_{ab}(\omega)$ is the (grounded) circuit Laplacian.

The most natural measurement on a circuit is the impedance response $Z_{ab}(\omega)$, which is the ratio of the voltage between two nodes a and b due to a current $I_j = I_0(\delta_{j,a} - \delta_{j,b})$, where δ is the Kronecker delta, that enters through a and exits at b. Mathematically, $Z_{ab}(\omega)$ simply involves the inversion of equation (11):

$$\begin{aligned} Z_{ab}(\omega) &= \frac{V_a - V_b}{I_0} \\ &= \sum_c \frac{G_{ac}(\omega)I_c - G_{bc}(\omega)I_c}{I_0} \\ &= G_{aa}(\omega) + G_{bb}(\omega) - G_{ab}(\omega) - G_{ba}(\omega) \\ &= \sum_n \frac{|\phi_n(a) - \phi_n(b)|^2}{j_n(\omega)} \end{aligned} \tag{12}$$

where $J_{ab}(\omega) = \sum_n j_n(\omega)|\phi_n(a)\rangle\langle\phi_n(b)|$ is the expansion of the Laplacian into its eigenmodes (the ω dependence of the eigenmodes is left implicit), with the Green's function $G_{ab}(\omega) = \sum_n \frac{1}{j_n(\omega)}|\phi_n(a)\rangle\langle\phi_n(b)|$ being its inverse. When the circuit is ungrounded, an overall shift of the potential cannot be detected, and the corresponding zero eigenspace should be excluded in the definition of the Green's function.

Equation (12) describes the impedance between any two nodes purely in terms of the eigenmodes and eigenvalues of the Laplacian. Most notably, it suggests that circuit resonances (divergences of the impedance) occur whenever there are non-trivial zero eigenvalues j_n. In a realistic circuit with unavoidable disorder, the strength of such resonances depends on the density of such zero eigenmodes, as well as whether there is any mechanism that pins them to zero.

A quintessential example of a strong protected resonance is a topolectrical resonance, which occurs due to topologically protected zero modes of the circuit Laplacian. Due to the localization of these modes at the boundary, such resonances can be easily identified through extremely large resonances at the boundary but not the interior of the circuit lattice. In this Article, the corner modes are such an example.

The circuit Laplacian in momentum space $\tilde{J}_\lambda(\omega_0, \mathbf{k})$ is given by

$$\begin{aligned} \tilde{J}_\lambda(\omega_0, \mathbf{k}) &= \sum_n e^{-i\mathbf{k}\cdot\mathbf{a}_n} J_{\mathbf{0}\mathbf{a}_n}(\omega_0) \\ &= i\sqrt{\frac{c}{l}}\,[(1+\lambda\cos k_x)\sigma_1\tau_0 \\ &\quad +(1+\lambda\cos k_y)\sigma_2\tau_2 \\ &\quad -\lambda\sin k_x\,\sigma_2\tau_3 \\ &\quad +\lambda\sin k_y\,\sigma_2\tau_1] \end{aligned} \tag{13}$$

where $\mathbf{a}_n$ are the unit cell lattice vectors of the model defined in equation (11) with $a \equiv \mathbf{0}$ as the reference point and $b \equiv \mathbf{a}_n$, where intra-unit-cell degrees of freedom remain implicit in the first line. It has, up to an overall factor of i, the same form as the model for an electric quadrupole insulator defined in ref. [20].

Mapping to an effective Dirac problem and boundary modes. In the main text, we showed that the admittance matrix $J(\omega_0)$ possesses the required symmetries to define the topological characteristics of a quadrupole insulator. In this section we demonstrate that in the corresponding dynamical matrix D, the same symmetry properties emerge for frequencies near ω_0, but are realized globally. We derive the effective Dirac form of the matrix D and show explicitly that it implies the existence of corner modes.

We denote by $\widetilde{C}(k_x, k_y)$ and $\widetilde{W}(k_x, k_y)$ the Fourier components of the matrices C and W defined in the main text for a circuit with periodic boundary conditions. To show that M_x and M_y defined in equation (8) are emergent symmetries of the dynamical matrix $\widetilde{D}(k_x, k_y) = \widetilde{C}^{-1/2}(k_x, k_y)\,\widetilde{W}(k_x, k_y)\,\widetilde{C}^{-1/2}(k_x, k_y)$, we note that the spectrum of $\widetilde{D}(k_x, k_y)$ is gapless for $\lambda = 1$, with a linear band-touching point near $(k_x, k_y) = (\pi, \pi)$, but is gapped for $\lambda \neq 1$. This motivated us to expand $\widetilde{D}(k_x, k_y)$ to linear order in $(1-\lambda)$ and the deviations (p_x, p_y) of $\mathbf{k}$ from $= (\pi, \pi)$. The resulting effective dynamical matrix $D(p_x, p_y)$ takes the Dirac form

$$\begin{aligned} D(p_x, p_y) &= \omega_0^2\sigma_0\tau_0 + \frac{\omega_0^2}{4}(p_x\sigma_2\tau_3 - p_y\sigma_2\tau_1) \\ &\quad + \frac{\omega_0^2}{4}(1-\lambda)(\sigma_1\tau_0 + \sigma_2\tau_2) \end{aligned} \tag{14}$$

where the term proportional to $(1-\lambda)$ is a mass term. The spectrum of $D(p_x, p_y)$ is symmetric about ω_0^2. This is a result of the chiral symmetry $\mathcal{C} = \sigma_3\tau_0$, which anticommutes with $D(p_x, p_y)$. If this symmetry is not broken by a boundary in the range of frequencies near ω_0, topological boundary modes will be pinned to the frequency ω_0.

We then search for an explicit analytical solution to the localized corner state within the respective Dirac equation. Without loss of generality we consider a corner to the upper right of the sample. To implement this in our formalism, we have to consider a real-space dependence of the Dirac mass term in equation (14). For simplicity, we set $\omega_0 = 2$ and remove the overall energy shift ω_0^2 from the Dirac operator. Furthermore, we substitute $(1-\lambda)\sigma_1\tau_0$ by $\Delta\sin\phi\sigma_1\tau_0$ and $(1-\lambda)\sigma_2\tau_2$ by $\Delta\cos\phi\sigma_2\tau_2$ so that the operator reads

$$D = p_x\sigma_2\tau_3 - p_y\sigma_2\tau_1 + \Delta(\sin\phi\sigma_1\tau_0 + \cos\phi\sigma_2\tau_2) \tag{15}$$

where $\phi = \pi/4$ and $\phi = -3\pi/4$ holds inside and outside of the material, respectively. With these values for ϕ, we have merely implemented the sign change in the Dirac mass term across the sample boundary. We now give ϕ a position dependence to model a corner. A corner geometry requires that ϕ varies continuously from $\phi = \pi/4$ to $\phi = -3\pi/4$ and back again as we go once around the corner in real space (starting from within the sample). The form of this interpolation is constrained by symmetry arguments. Note that the bulk symmetries M_x, M_y and C_4 are all broken locally by the corner. The only symmetry that leaves the corner invariant is the diagonal mirror symmetry $M_{xy} = C_4M_x$, which sends $(x, y) \to (-y, -x)$ and is represented by

$$M_{xy} = \frac{1}{2}(\sigma_0 + \sigma_3)\tau_3 + \frac{1}{2}(\sigma_0 - \sigma_3)\tau_1 \tag{16}$$

The system respects chiral symmetry for any choice of ϕ.

Topological index: Mirror-graded winding number. Here we define the bulk topological invariant for a topological quadrupole insulator as a mirror-symmetry graded winding number. This index is valid if the model has diagonal mirror symmetry (for example, M_{xy}) and chiral symmetry $\mathcal{C}$. The latter is in any case required to pin topological corner modes to eigenvalue zero. Our topological invariant, which has already been employed[27] to characterize crystalline topological superconductors, is complementary to the characterization of multipole insulators in terms of Wilson loops that was given in ref. [20].

Consider a $\mathbf{k}$-dependent matrix (for example, a Bloch Hamiltonian, or an admittance matrix) $R(\mathbf{k})$ that both obeys $\mathcal{C}$ (that is, $\mathcal{C}R(\mathbf{k})\mathcal{C}^{-1} = -R(\mathbf{k})$) and M_{xy} (that is, $M_{xy}R(k_x, k_y)M_{xy}^{-1} = R(-k_y, -k_x)$) and let $[\mathcal{C}, M_{xy}] = 0$. The occupied bands of $R(k, k)$ can then be divided into subspaces with mirror eigenvalues ± 1 (or $\pm i$ for spinful mirror symmetry). Using this grading, we can bring $R(k, k)$ to the form

$$R(k,k) = \begin{pmatrix} 0 & q_+(k) & 0 & 0 \\ q_+(k)^\dagger & 0 & 0 & 0 \\ 0 & 0 & 0 & q_-(k) \\ 0 & 0 & q_-(k)^\dagger & 0 \end{pmatrix} \tag{17}$$

where the first half acts on the $+1$ mirror subspace, whereas the second half acts on the -1 mirror subspace. For $R(k, k)$ to be gapped, all eigenvalues of $q_\pm(k)$ need to be nonzero. We can thus define a 'spectrally flattened' pair of unitary matrices $\tilde{q}_\pm(k)$ which share the eigenstates and phase of the eigenvalues with $q_\pm(k)$, but have eigenvalues of absolute value 1. We can now define the winding numbers

$$\nu_\pm := \frac{i}{2\pi}\int_0^{2\pi} dk \mathrm{tr}\tilde{q}_\pm^\dagger(k)\partial_k\tilde{q}_\pm(k) \tag{18}$$

which are quantized to be integers († denotes the conjugate transpose). For a system with vanishing dipole moment, the net winding number $\nu_+ + \nu_-$ must vanish

in any direction of momentum space. Hence, for the systems of interest to us $\nu_+ = -\nu_-$, and we can use

$$\nu := \frac{\nu_+ - \nu_-}{2} \in \mathbb{Z} \tag{19}$$

as a topological invariant. The number of topological corner modes is equal to the parity of ν.

We now demonstrate this topological invariant for the admittance matrix realized in our electrical circuit. Up to prefactors, the matrix takes the form

$$\begin{aligned} R(\mathbf{k}) &= (1+\lambda\cos k_x)\sigma_1\tau_0 \\ &\quad +(1+\lambda\cos k_y)\sigma_2\tau_2 \\ &\quad -\lambda\sin k_x\sigma_2\tau_3 \\ &\quad +\lambda\sin k_y\sigma_2\tau_1 \end{aligned} \tag{20}$$

and $\mathcal{C}=\sigma_3\tau_0$, with $M_{xy}=\frac{1}{2}(\sigma_0+\sigma_3)\tau_3+\frac{1}{2}(\sigma_0-\sigma_3)\tau_1$. The mirror-eigenvalue graded off-diagonal components of $R(k, k)$ are scalars in this case and can be computed as

$$q_\pm(k) = \sqrt{2}\,(1+\lambda e^{\mp ik}) \tag{21}$$

Clearly, for $\lambda > 1$, they have winding number $\nu_\pm = \pm 1$ and thus $\nu = +1$, corresponding to the topologically non-trivial phase with corner modes. In contrast, for $\lambda < 1$ we find $\nu_\pm = 0$ and thus $\nu = 0$, corresponding to the topologically trivial phase.

Dipole and quadrupole polarization. In this section, we present how the dipole and quadrupole topological polarization can be expressed in terms of Bloch eigenfunctions and the Berry connection.

Dipole polarization, Wannier functions and projected density operator. In the continuum, the dipole polarization $p_a = \int x_a \rho(\mathbf{x})\mathrm{d}\mathbf{x}$ gives us the expectation value of the centre of mass with respect to a density operator ρ. On a two-dimensional lattice, its definition should be modified in two ways. First, ρ should be replaced by the band projector $P = \sum_{n,\mathbf{k}} |u^n_\mathbf{k}\rangle\langle u^n_\mathbf{k}|$, where $|u^n_\mathbf{k}\rangle = u^n_\mathbf{k}\,|\mathbf{k}\rangle$ is the nth occupied Bloch eigenstate with quasimomentum $\mathbf{k}=(k_x, k_y)$. Second, considering only the x direction and omitting the component index a, x should be replaced by the periodic position operator $\widehat{X} = e^{2\pi i\hat{x}/L_x} = \sum_x e^{2\pi i x/L_x}\,|x\rangle\langle x|$, where $|x\rangle$ denotes a state at site x and L_x is the total number of sites. We can thus rewrite the polarization operator as

$$\begin{aligned} \tilde{\rho} &= P\widehat{X}P \\ &= Pe^{iQ\hat{x}}P \end{aligned} \tag{22}$$

which may also be interpreted as the projected density operator at momentum $Q = \frac{2\pi}{L_x}$. When P trivially projects onto all bands, $\tilde{\rho} = \widehat{X}$ simply gives the periodic position. When P is non-trivial, the eigenvalues and eigenvectors of $\tilde{\rho}$, respectively, give the polarization spectrum and Wannier functions. It is well known that the polarization spectral flow tells us the net number of edge modes leaving the band(s). Note that these edge modes exist even in classical lattice systems, where band projectors cannot be physically realized as filled Fermi seas.

Since the density operator satisfies

$$e^{iQ\hat{x}} = \sum_\mathbf{k} |\mathbf{k}+Q\hat{\mathbf{e}}_x\rangle\langle\mathbf{k}| \tag{23}$$

the projected density operator takes the form

$$\begin{aligned} \tilde{\rho} &= \sum_{n,m,\mathbf{k}} |u^n_{\mathbf{k}+Q\hat{\mathbf{e}}_x}\rangle\langle u^n_{\mathbf{k}+Q\hat{\mathbf{e}}_x}\,|u^m_\mathbf{k}\rangle\langle u^m_\mathbf{k}| \\ &\approx \sum_{n,m,\mathbf{k}} [e^{iQA_x(\mathbf{k})}]_{nm}\,|u^n_{\mathbf{k}+Q\hat{\mathbf{e}}_x}\rangle\langle u^m_\mathbf{k}| \end{aligned} \tag{24}$$

with equality in the $L_x \to \infty$ limit. In this limit, the matrix $U_{nm}(\mathbf{k}) = \langle u^n_{\mathbf{k}+Q\hat{\mathbf{e}}_x}|\,u^m_\mathbf{k}\rangle$ is unitary and tends towards $[e^{iQA_x(\mathbf{k})}]_{nm}$, where $A_x(\mathbf{k}) = -i\langle u^n_\mathbf{k}\,|\partial_{k_x}u^m_\mathbf{k}\rangle$ is the non-Abelian Berry connection. In this form, it is easy to guess the form of eigenvectors $|W^s_{k_y}\rangle$ of $\tilde{\rho}$, which are also known as the Wannier functions. Note that k_x no longer enters as an index, since $\tilde{\rho}$ is not diagonal in it. As $\tilde{\rho}$ implements both the momentum translation $\mathbf{k}\to\mathbf{k}+Q\hat{\mathbf{e}}_x$ and the internal rotation $U_{nm}(\mathbf{k})$, an eigenvector must contain compensatory factors such that it transforms covariantly under simultaneous translation and rotation. For this, it should be proportional to the Wilson line $\Phi(k_x, k_y) = U(0, k_y)\ldots U(k_x - Q\hat{\mathbf{e}}_x, k_y)\,U(k_x, k_y) = \mathcal{P}e^{i\int_0^{k_x} A_x(p_x,k_y)\mathrm{d}p_x}$, where $\mathcal{P}$ is the path-ordering operator, as well as a power of e^{-ik_x}:

$$\begin{aligned} |W^s(k_y)\rangle &= \sum_{k_x} e^{-ik_x\theta_s(k_y)/(2\pi)}\Phi(k_x,k_y)\,|W^s_0(k_y)\rangle \\ &= \sum_{m,n,k_x} e^{-ik_x\theta_s(k_y)/(2\pi)}[\Phi(k_x,k_y)]_{mn} \\ &\quad \times|u^m_\mathbf{k}\rangle\langle u^n_\mathbf{k}|\;W^s_0(k_y)\rangle \end{aligned} \tag{25}$$

Since the right-hand side of equation (26) should be invariant under $k_x \to k_x + 2\pi$, it follows that $e^{i\theta_s(k_y)}$ and $|W^0_s(k_y)\rangle$ are, respectively, the eigenvalues and eigenvectors of the Wilson loop operator

$$\Phi(2\pi, k_y) = \mathcal{P}e^{i\oint_0^{A_x(p_x,k_y)dp_x}} \tag{26}$$

Through direct substitution of equation (26) into equation (24) it may then be verified that the eigenvalues of $|W^s(k_y)\rangle$ are given by $e^{i\theta(k_y)/L_x}$.

To summarize, the Wilson loop operator $\Phi(2\pi, k_y)$ is closely related to the projected density operator $\tilde{\rho}$, which is also diagonal in k_y. Their eigenvalues are given by $e^{i\theta(k_y)}$ and $e^{i\theta(k_y)/L_x}$, respectively. Given an eigenvector $|W^s_0(k_y)\rangle$ of $\Phi(2\pi, k_y)$, one can construct the eigenvector $|W^s(k_y)\rangle$ of $\tilde{\rho}$ via equation (26). However, to do so, knowledge of the Wilson line $\Phi(k_x, k_y)$ at all k_x is required. In this sense, the physical polarization eigenvectors (Wannier functions) carry 'more' information than can be obtained from the Wilson loop alone.

Nested Wilson loop and quadrupolar polarization. If the Wannier polarization ($\tilde{\rho}$) spectrum is gapped, one can perform a nested Wilson loop computation to reveal a possible quadrupole moment.

In general, the total polarization is given by $-i\log\mathrm{tr}\Phi$, where Φ is the Wilson loop operator. In the nested Wilson loop computed over the eigenstates $|W^s(k_y)\rangle$ of $\tilde{\rho}$, the gapped cases allow evaluation of the polarization of one sector at a time, where the total polarization simplifies to

$$\begin{aligned} p^s &= -\frac{1}{(2\pi)^2}\mathrm{tr}\int_{\mathrm{BZ}} A^s_y(\mathbf{k})\mathrm{d}^2\mathbf{k} \\ &= i\frac{1}{(2\pi)^2}\mathrm{tr}\int_{\mathrm{BZ}}\langle W^s(k_y)\;|\partial_{k_y}W^s(k_y)\rangle\mathrm{d}^2\mathbf{k} \end{aligned} \tag{27}$$

where BZ denotes the Brillouin zone and $A^s_y(\mathbf{k})$ is the Berry connection of $|W^s(k_y)\rangle$. To express p^s explicitly in terms of the Berry connections A_x, A_y of the original Bloch eigenstates $|u^m_\mathbf{k}\rangle$, one notes that if $|W^s(k_y)\rangle = \sum_m M^{ms}_\mathbf{k}\,|u^m_\mathbf{k}\rangle$,

$$\begin{aligned} p^s &= -\frac{1}{(2\pi)^2}\mathrm{tr}\int_{\mathrm{BZ}}[(MM^\dagger)A_y - iM^\dagger\partial_{k_y}M]\mathrm{d}^2\mathbf{k} \\ &= \frac{i}{(2\pi)^2}\int_{\mathrm{BZ}}\left[\sum_{mm'}(M^{m's}_\mathbf{k})^*\langle u^{m'}_\mathbf{k}\,|\partial_{k_y}u^m_\mathbf{k}\rangle M^{ms}_\mathbf{k}\right. \\ &\quad \left. +\sum_m (M^{m's}_\mathbf{k})^*\partial_{k_y}M^{ms}_\mathbf{k}\right]\mathrm{d}^2\mathbf{k} \end{aligned} \tag{28}$$

where, from equation (26),

$$M^{ms}_\mathbf{k} = \sum_{k_x} e^{-ik_x\theta_s(k_y)/(2\pi)}\langle u^m_\mathbf{k}|\;\Phi(k_x,k_y)\;|W^s_0(k_y)\rangle \tag{29}$$

with $\Phi(k_x, k_y) = \mathcal{P}e^{i\int_0^{k_x}A_x(p_x,k_y)\mathrm{d}p_x}$, and $e^{i\theta_s(k_y)}$ and $|W^s_0(k_y)\rangle$ being the sth eigenvalue and eigenvector of $\Phi(2\pi, k_y)$.

Multipolar polarizations in a classical environment. As seen above, the topological nature of a band system is fundamentally encoded in its band projectors. But unlike fermionic quantum systems with occupied Fermi seas, there is no Pauli principle for classical excitations in a circuit (but see ref. [28] for a demonstration of wavepacket pumping in optical systems) and the band projector does not have a direct physical interpretation. To understand how bulk topological polarization is indirectly but faithfully manifested in a classical circuit, we first connect topological boundary modes with band projectors by observing that they, by virtue of residing within the bulk gap, are necessarily properties of projectors that demarcate a set of negative eigenvalue bands of the impedance operator $\hat{J}$ from its complement. Indeed, the electric polarization in the x direction of a crystal is given by the spectral flow of the eigenspectrum of the density operator[29,30] $\tilde{\rho} = \widehat{P}e^{i2\pi\hat{x}/L_x}\widehat{P}$, with $\widehat{P}$ the projector onto the filled subspace of bulk bands. To identify this spectral flow with physical quantities, we consider the adiabatic deformation

$$e^{i2\pi\hat{x}/L_x} \to \widehat{R} \tag{30}$$

where $\widehat{R}$ is the projector onto a real-space region R. Under this deformation to the operator $\widehat{P}\widehat{R}\widehat{P}$, the initially equally spaced polarization bands adiabatically accumulate near 1 and 0, the eigenvalues of $\widehat{R}$, with the exception of those that traverse this interval due to non-trivial spectral flow.

The next observation is that, since $\widehat{P}$ and $\widehat{R}$ are projectors, $\widehat{P}\widehat{R}\widehat{P}$ and $\widehat{R}\widehat{P}\widehat{R}$ have identical non-trivial eigenvalues and eigenmodes[30]. Now, $\widehat{R}\widehat{P}\widehat{R}$ is the band projector $\widehat{P}$ projected onto region R (that is, with open boundary conditions). A further adiabatic interpolation

$$RPR \to RJR \tag{31}$$

completes the deformation to the Laplacian with open boundary conditions $\widehat{R}\hat{J}\widehat{R}$. Importantly, midgap states in the polarization spectrum are adiabatically mapped to midgap states in the Laplacian spectrum. Since midgap states exist within a bulk gap they must necessarily be boundary states.

Through this series of deformations, we can re-interpret real-space polarization as polarization in 'admittance-space' (that is, along the axis where eigenvalues of the Laplacian J reside). This re-interpretation involves fundamentally interchanging the roles of position and momentum, which exchanges the projectors $\widehat{R}$ and $\widehat{P}$. In this way, the mathematical operation of projection onto the Fermi sea is replaced by that of implementing open boundary conditions, hence allowing the topological properties of classical systems to be studied on the same footing as those of quantum systems.

Hence, to summarize, the 'dipole moment' for dipole polarization is classically manifested as the existence of midgap states that, by definition, are necessarily 'polarized' at the boundary. This holds analogously for quadrupole moments, as detailed in the section 'Nested Wilson loop and quadrupolar polarization'.

Data availability. The data that support the plots within this paper and other findings of this study are available from the corresponding author upon reasonable request.

References

27. Zhang, F., Kane, C. L. & Mele, E. J. Topological mirror superconductivity. *Phys. Rev. Lett.* **111**, 056403 (2013).
28. Wimmer, M., Price, H. M., Carusotto, I. & Peschel, U. Experimental measurement of the Berry curvature from anomalous transport. *Nat. Phys.* **13**, 545–550 (2017).
29. Fidkowski, L., Jackson, T. & Klich, I. Model characterization of gapless edge modes of topological insulators using intermediate Brillouin-zone functions. *Phys. Rev. Lett.* **107**, 036601 (2011).
30. Lee, C. H. & Ye, P. Free-fermion entanglement spectrum through Wannier interpolation. *Phys. Rev. B* **91**, 085119 (2015).